4.5 DEFECT EVOLUTION IN NEUTRON-IRRADIATED SINGLE CRYSTALLINE TUNGSTEN – X. Hu, T. Koyanagi, Y. Katoh (Oak Ridge National Laboratory), M. Fukuda (Tohoku University), B.D. Wirth, L.L. Snead (University of Tennessee, Knoxville)

OBJECTIVE

The objective of this work is to investigate the microstructural defect evolution and the resulting mechanical property changes in neutron irradiated single crystalline tungsten to facilitate the development of plasma-facing materials for fusion reactors.

SUMMARY

High purity <110> single crystalline tungsten samples were examined by positron annihilation spectroscopy following low temperature and low dose neutron irradiation and subsequent isochronal annealing. The results were used to determine microstructural and defect evolutions, thus, identifying the annealing mechanisms. The one-hour isochronal annealing was performed on two specimens neutron-irradiated to very low (0.006) and low (0.03) dpa at ~90°C. Following annealing at 400, 500, 650, 800, 1000, 1150, and 1300°C, *ex-situ* characterization of vacancy defects used positron lifetime spectroscopy and coincidence Doppler broadening (CDB). Vacancy cluster size distributions showed significant damage recovery around 1000°C, consistent with Stage III below 400°C and Stage V temperature around 1000°C. CDB results confirmed the trend of the vacancy defect evolution and S-W plots confirmed a single type of vacancy clusters. This microstructure information is consistent with the measured hardness changes.

PROGRESS AND STATUS

Introduction

Numerous studies have explored the recovery processes of radiation-induced damage in tungsten. Residual electrical resistivity was commonly used as an index of the damage present in materials for the damage recovery study, resulting in the identification of the temperatures and activation energies for different annealing stages. Early studies on neutron-irradiated tungsten [1-5] demonstrated five damage recovery stages by using resistivity measurement. Stage I occurs below −170°C, attributing to the migration of self-interstitials. Stage II, covering a broad temperature regime, −170~350°C, results from the thermal activation of interstitials from traps with activation energies from 0.25 to 1.7 eV. Stage III (~ 0.15 T_m/350°C), Stage IV (~ 0.22 Tm/640°C), and Stage V (0.31 Tm/970°C) were also identified. To date, the physical mechanisms governing the damage recovery in these five stages are still controversial. In this work, single crystalline tungsten samples following low dose and low temperature neutron irradiation were investigated to explore the radiation damage evolution at different annealing stages and to link them with the observed microstructure and the hardness at different annealing conditions.

Experiment

Neutron irradiation of the specimens was carried out in the flux trap facility in HFIR at a temperature of 90 ± 10°C. The two specimens studied here, 1W05 and 1W25, were irradiated to fast neutron fluences of 2×10^{23} and 1×10^{24} n/m^2 (E>0.1 MeV) equivalent to displacement damage levels of ~0.006 dpa and ~0.03 dpa, respectively. Following the isochronal annealing for one hour at 400, 500, 650, 800, 1000, 1150, and 1300°C, *ex-situ* characterization of vacancy defects was performed using positron annihilation spectroscopy (PAS). Micro-hardness tests were also conducted after each annealing step using a micro-Vickers indentor at a load of 1.96 N.

Results

Positron Annihilation Lifetime Spectroscopy

Subsequent to each annealing step, PAS measurement was conducted. To illustrate directly the influence of annealing temperature on the measured positron lifetime data, the normalized spectra obtained for specimens 1W05 and 1W25 at seven annealing conditions together with the as-received and as-irradiated conditions are shown in Figure 1. The annealing processes of 1W05 and 1W25 involve some common features. Clearly, the long lifetime components of the spectra become more intense after irradiation. The spectra for the annealing temperatures 400, 500, 650, and 800°C are difficult to distinguish, but have more significant long lifetime components compared to the as-irradiated samples. Subsequently, the lifetime spectra start to shift to the shorter lifetimes after the 1000°C anneal, closer to the spectra of unirradiated samples. This shows qualitatively that the density and the size of the vacancy clusters evolve during the isochronal annealing process.

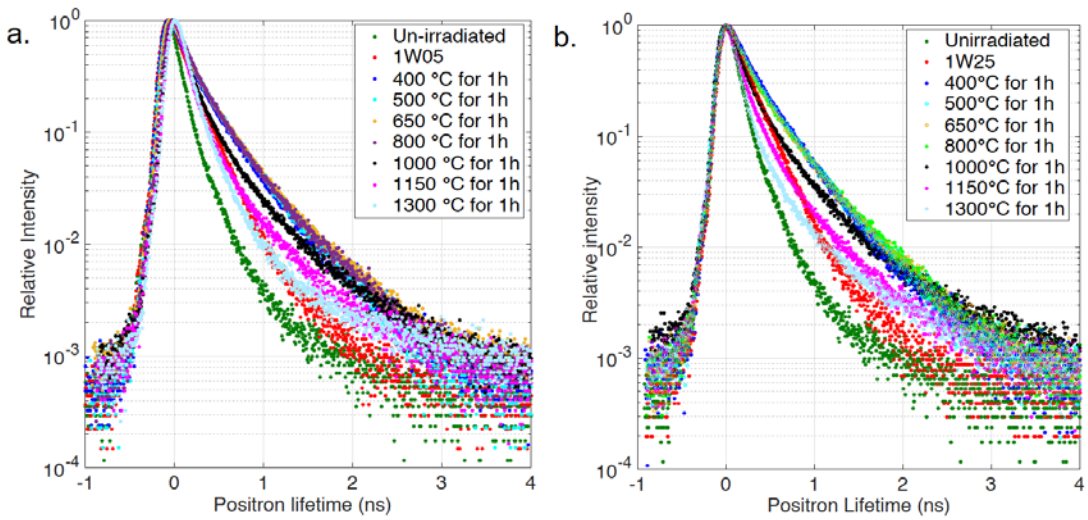

Figure 1. Positron lifetime spectra for annealed tungsten (a) 1W05 and (b) 1W25. Spectra for un-irradiated and as-irradiated tungsten samples are also shown for comparison.

In the present study, the measured positron lifetime spectra for tungsten could be resolved into three lifetime components by applying the trapping model. The results of the analysis are shown in Figure 2. τ_1 and I_1 indicate the lifetime and relative intensity of the positrons annihilated in the bulk lattice. The two long lifetimes, τ_2 and τ_3 and their associated intensity I_2 and I_3 arise from the positrons trapped in the 3D vacancy clusters. For the un-irradiated samples, the presence of single vacancies and nano-voids were observed but in relatively small fractions (23% and 7%, respectively). τ_2 increased to ~230 ps for both 1W05 and 1W25 subject to neutron irradiation, equivalent to a complex containing 2~3 vacancies, along with a significant increase in intensity, indicating that a large amount of small vacancy clusters were induced by neutron irradiation. In contrast, the τ_3 had a small increase and the change for I_3 was negligible. The higher does level of 1W25 implied a larger mean positron lifetime in comparison with 1W05, as shown in Figures 2(a) and (c).

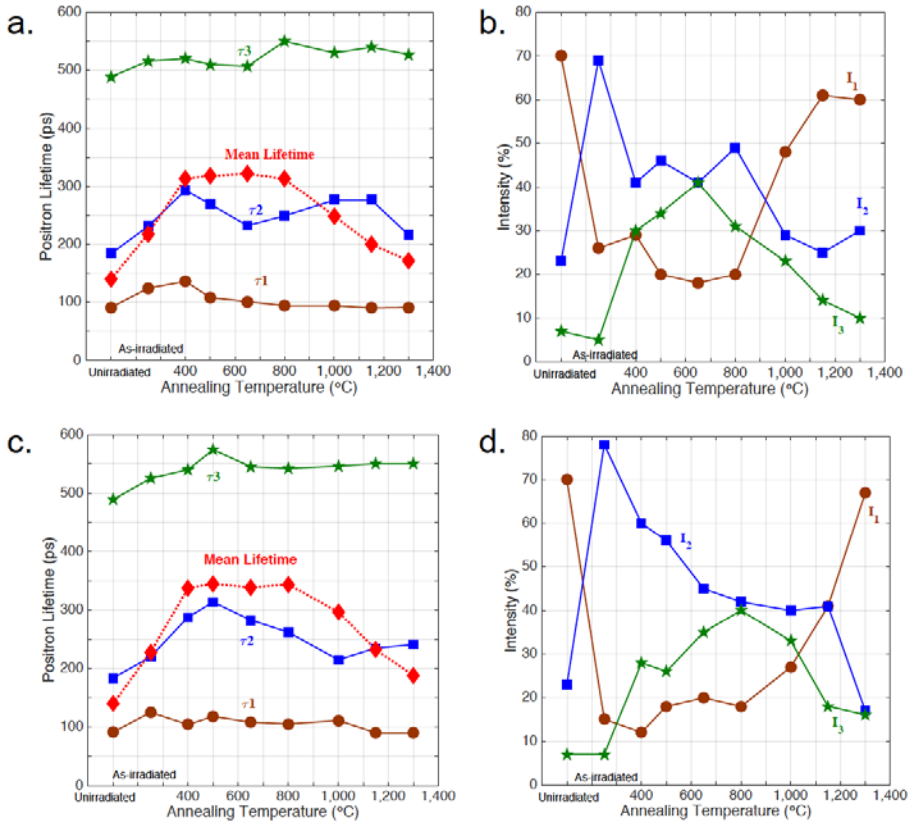

Figure 2. Positron lifetimes (a, c) and their intensities (b, d) as functions of annealing conditions for 1W05 (a, b) and 1W25 (c, d). The dashed lines in (a) and (c) indicates the mean lifetimes for these two samples at different annealing stages.

The changes of the PAS parameters in different temperature ranges reflect the microstructural defect evolutions during annealing. As shown in Figure 2(a) and (c), the mean positron lifetime showed a quite similar trend for both samples and provided a rough identification of different annealing stages. After annealing at 400°C, the mean lifetime increased and then kept at a constant value up to 800°C annealing. Subsequently, it started to drop after being annealed at 1000°C, when the emission of single vacancy from thermal dissociation of large vacancy clusters and the annihilation of mobile vacancy clusters at sinks were becoming significant.

The analysis of two longer exponents yielded more detailed microstructural information as following. The presence of τ_2 and τ_3 demonstrated the presence of small vacancy clusters and nano-voids. The lifetime, $\tau_2 \sim 200 - 314\, ps$, is equivalent to average cavity sizes of ~1−9 vacancies and the longest lifetime of ~550 ps is associated with voids containing more than 40 vacancies. After annealing at 400°C for both samples, τ_2 is increasing, indicating the growth of small vacancy clusters due to the mobile single vacancy, which is consistent with the previous definition of Stage III (~0.15 T_m/350°C) [3]. In the anneal stages of 400−650°C for 1W05 and 400−800°C for 1W25, although the mean lifetime had negligible change, I_2, the intensity of τ_2, which is corresponding to the number density of small vacancy clusters, decreased, while the number density of voids increased. In this stage, the growth of voids is at the expense of small vacancy clusters. The strong coarsening of the nano-void population implied the stage IV, 650−800°C, caused by the migration and coalescence of the existing vacancy clusters. In the annealing stages above 800°C for 1W05 and above 1000°C for 1W25, the significant vacancy dissociation from nano-voids and voids yielded a strong reduction of the populations of these defects, named as Stage V. When the annealing temperature increased above stage V, I_3 dropped abruptly while I_2 had a general decrease trend. After the 1300°C annealing, the impurity stabilized vacancy clusters

contributed to the observation of I_2 [4]. The significant drop of void population at this stage was likely induced by coarsening of the void population due to Ostwald ripening or the dissociation of the voids [6, 7].

Coincidence Doppler Broadening

Positrons injected into materials eventually annihilate with electrons, producing predominantly two gamma rays travelling in approximately opposite directions, necessitated by energy-momentum conservations during annihilation. The total energy of the annihilation gamma rays is given by $2m_0c^2 - E_B$, where m_0c^2 is the electron rest mass energy and E_B is the electron binding energy. Since there is a net center of mass energy associated with the annihilating positron-electron pair, the total energy will not split equally for the two gamma rays. One gamma ray is upshifted and the other is downshifted. The energy shift of each photon is given by

$$\Delta E=\frac{1}{2}p_L c=\frac{1}{2}\theta_L m_0 c^2 \quad (1)$$

where ΔE is the photon energy difference from the nominal value, p_L is the corresponding longitudinal momentum shift along the direction of gamma ray emission, in atomic unit (1 a.u.=7.28 mrad×m_0c), θ_L is the angular deviation of the photons from 180°. Since p_L has element specific spectral distributions that correspond to the momentum distributions of the annihilation electrons, analysis of the orbital electron momentum spectrum (OEMS) provides information on the defects. The OEMS is typically represented as the fraction of annihilations at each momentum interval as a function of p_L, normalized by a standard spectrum. It is more convenient to represent OEMS data in so called *S−W* plots. The S is a fraction of low-momentum annihilation defined by specified p_L region, which in this study is $p_L \leq 0.382\ a.u.$, and W is the corresponding high-momentum annihilation fraction, defined as $1.0\ a.u. \leq p_L \leq 4.0\ a.u.$. A particular microstructure produces a point on a *S−W* plot. *S−W* correlation plots are useful in detecting the change in the nature of the positron trapping defects, since the slope of the plot is a fingerprint of a specific vacancy.

Figure 3 shows the $n(p_L)/n_W(p_L)$ OEMS obtained as a function of annealing temperature for 1W05 and 1W25. The basic principle to understand this plot is that damaged materials gave rise to the enhancement of the low momentum fraction due to the higher possibility of being annihilated by valence electrons for positrons. As shown in Figure 3, the increase of low momentum part and decrease of high momentum part indicated that intense damage was induced in tungsten subject to neutron irradiation for both samples. The OEMS curves for annealing processes at the temperatures lower than 1000°C overlapped without obvious changes, while the low momentum parts were enhanced and high momentum parts were weakened in comparison with the as-irradiated conditions. The subsequent high temperature annealing (1000°C, 1150°C, and 1300°C) promoted damage recovery, driving the OEMS curves close to the non-irradiated W.

S-W plots could be obtained from the OEMS plots based on the definition of different momentum windows for S and W, shown in Figure 4. Each data point in Figure 4 refers to one specific microstructure following the corresponding annealing process. Larger low momentum fraction and smaller high momentum fraction refers to the more damaged microstructure. It is apparent that the pathways of the data points are consistent with the materials responses to annealing shown in the normalized OEMS plots. Significant damage recovery was observed after annealing at 1000°C for both 1W05 and 1W25. The circled S-W data points in Figure 4 indicated that the overall microstructure had insignificant evolution at the annealing stages lower than 1000°C. As can be seen from Figure 4, the linear relationship between S and W demonstrated only one type of vacancy-type defects dominated in both 1W05 and 1W25 following different annealing conditions. The identical slope for these two samples implies that transmutation elements produced by neutron irradiation are negligible for such small dose level. The dominant positron trapping sites are solely W-vacancy clusters for both 1W05 and 1W25.

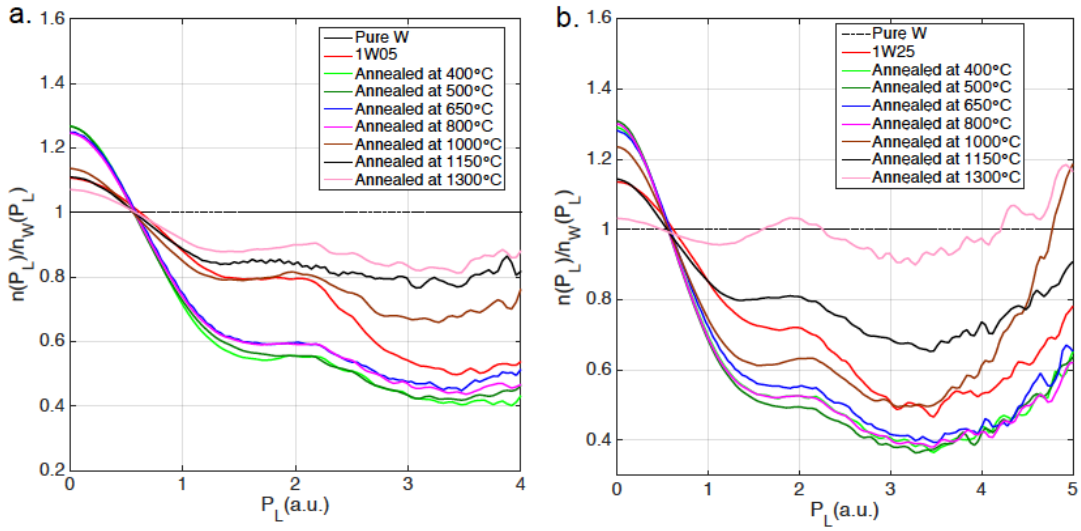

Figure 3. Normalized OEMS of 1W05 and 1W25 in different annealing conditions. The correspondingly normalized curves for as-received and as-irradiated conditions are also shown for comparison.

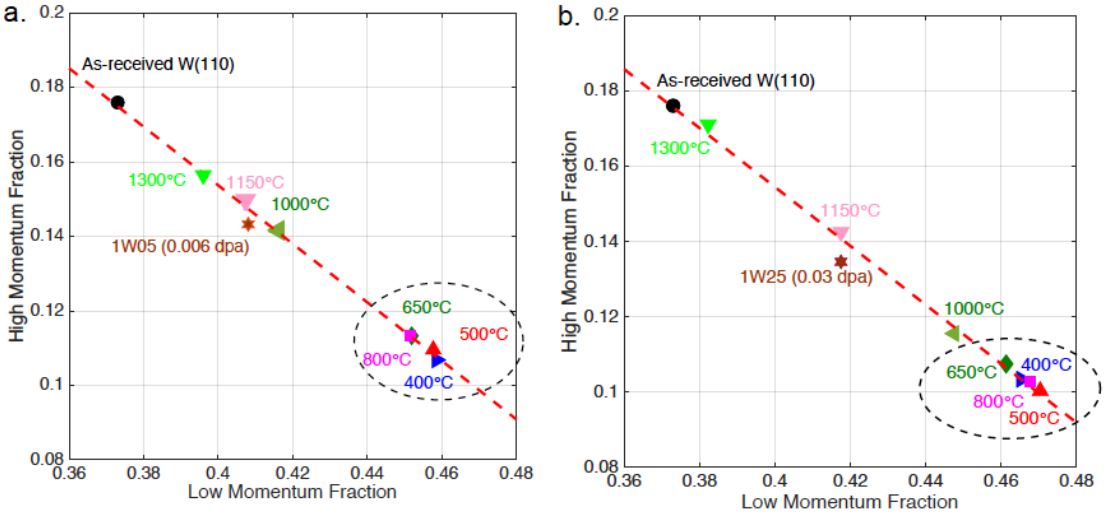

Figure 4. S-W plots for (a) 1W05 and (b) 1W25 during the annealing process. Positron annihilation fraction in the high momentum region ($\mathbf{1.0\ a.u.} \leq \boldsymbol{p_L} \leq \mathbf{4.0\ a.u.}$) versus the low momentum region ($\boldsymbol{p_L} \leq \mathbf{0.382\ a.u}$). The dashed lines are drawn to guide eyes.

<u>Mechanical Property Characterization</u>

In response to the defect damages inside tungsten, its mechanical properties are expected to change during the annealing processes. Embrittlement is one of the most significant degradation phenomena for tungsten exposed to irradiation and impacts the tungsten's service life and performance in the application of PFM. During the annealing process, microstructures of the studied samples evolve, and the corresponding mechanical property change occurs. Hardness of the studied samples, as a factor contributing to irradiation embrittlement, was determined by micro-Vickers testing following each annealing condition, as shown in Figure 5. Overall, significant hardening was observed after annealing stages at temperatures below 800°C while softening occurred for the annealing stages with temperatures

higher than 1000°C. Similar to the tensile tests, the observed hardness change could be linked to the microstructure evolution. It is known that the hardness (H_v) is roughly proportional to the yield stress (τ_y), [8], therefore,

$$\Delta H_V \propto \Delta\tau_y \propto \alpha(Nd)^{1/2}. \quad (2)$$

While the interstitial clusters are obstacle to the mobile dislocations, the hardness is dominated by the vacancy defects due to the facts that the concentration of interstitial clusters is by several orders of magnitude lower than that of vacancy defects as well as that vacancy clusters are much stronger obstacles [9].

Hardness of both samples increased after neutron exposure in Figure 5. The absolute increase values of hardness for 1W05 and 1W25 were quite close with a slightly higher value for 1W25. The increase of defect population observed in PALS also showed a similar tendency. This observation indicated that although the irradiation dose of 1W25 is five times of that of 1W05, the resulting displacement damage is not proportional to the radiation level.

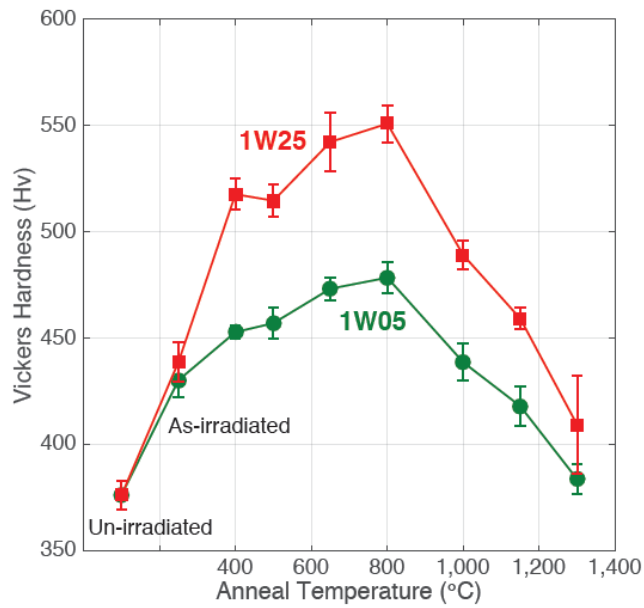

Figure 5. Vickers hardness for 1W05 and 1W25 following different annealing conditions. The hardness values for un-irradiated and as-irradiated samples are also shown for comparison.

As shown in Figure 5, significant hardening was observed after annealing stages at temperatures below 800°C, although the overall concentration of vacancy clusters decreased. It is noted that the consequential hardness results from the collective contributions of all kinds of defects involved. Eq. 21 implies that the competition of strength factor, defect size and concentration determines the hardness. When temperature was lower than 800°C, the concentration of small vacancy clusters (i.e., monovacancy) reduced dramatically, the intermediate vacancy clusters had insignificant changes, and large vacancy clusters (i.e., cavity) has an obvious trend to grow for both samples. It is known that the strength factor of vacancy defects is a function of defect size [9]. The strength factor of big cavities could be several orders higher than that of a monovacancy. The annealing hardening observed in Figure 5 was ascribed mainly to the growth of cavities, resulting from the mobility of single vacancy and small vacancy clusters. Starting from the 1000°C annealing, sample softening showed up due to the significant damage recovery. The growth of big cavities was suppressed by the dissociation process driven by high temperatures. Therefore, the reduction of defect population gave rise to the softening. Note that the measured hardness of both samples following the 1300°C anneal was still higher than that of un-irradiated tungsten samples, which indicated that radiation-induced damage was not completely recovered, consistent with the PAS results.

References

[1] Thompson, M.W., The damage and recovery of neutron irradiated tungsten. Philosophical Magazine, 1960. 5(51): p. 278-296.

[2] Keys, L.K., J.P. Smith, and J. Moteff, High-Temperature Recovery of Tungsten after Neutron Irradiation. Physical Review, 1968. 176(3): p. 851-856.

[3] Keys, L.K. and J. Moteff, Neutron irradaition and defect recovery of tungsten. Journal of Nuclear Materials, 1970. 34: p. 260-280.

[4] Kim, Y.-W. and J.M. Galligan, Radiation damage and stage III defect annealing in thermal neutron irradiated tungsten. Acta Matallurgica, 1978. 26: p. 379-390.

[5] Kim, Y.-W. and J.M. Galligan, An annealing study of thermal neutron irradiated tungsten. Journal of Nuclear Materials, 1978. 69&70: p. 680-682.

[6] Eldrup, M. and B.N. Singh, Study of defect annealing behavior in neutron irradiated Cu and Fe using positron annihilation and electrical conductivity. Journal of Nuclear Materials, 2000. 276: p. 269-277.

[7] Eldrup, M. and B.N. Singh, Accumulation of point defects and their complexes in irradiated metals as studied by the use of positron annihilation spectroscopy – a brief review. Journal of Nuclear Materials, 2003. 323(2-3): p. 346-353.

[8] Busby, J.T., M.C. Hash, and G.S. Was, The relationship between hardness and yield stress in irradiated austenitic and ferritic steels. Journal of Nuclear Materials, 2005. 336(2-3): p. 267-278.

[9] Hu, X., et al., Modeling of irradiation hardening of iron after low-dose and low-temperature neutron irradiation. Modelling and Simulation in Materials Science and Engineering, 2014. 22(6): p. 065002.